

A computational analysis of binding modes and conformation changes of MDM2 induced by p53 and inhibitor bindings

Jianzhong Chen · Jinan Wang · Weiliang Zhu ·
Guohui Li

Received: 20 August 2013 / Accepted: 17 November 2013 / Published online: 22 November 2013
© Springer Science+Business Media Dordrecht 2013

Abstract Molecular dynamics (MD) simulations followed by principal component analysis were performed to study the conformational change of MDM2 induced by p53 and two inhibitor (P4 and MI63a) bindings. The results show that the hydrophobic cleft of MDM2 is very flexible and adaptive to different structural binding partners. The cleft tends to become wider and more stable as MDM2 binds to the three binding partners, while unbound MDM2 shows a narrower and pretty flexible cleft, which agrees with recent experimental data and theoretical studies. It was also found that the binding of P4 and p53 stabilizes the motion of the loop L2 linking the helix $\alpha 2$ and β strand ($\beta 3$), but the presence of MI63a makes the motion of L2 disordered. In addition, the binding free energies of the three partners to MDM2 were calculated using molecular mechanics generalized Born surface area to explain the binding modes of these three partners to MDM2. This study will be helpful not only for better understanding the functional, concerted motion of MDM2, but also for the rational design of potent anticancer drugs targeting the p53–MDM2 interaction.

Keywords p53–MDM2 interaction · Molecular dynamics simulation · PCA · MM-GBSA

Introduction

Important functions of the tumor suppressor p53 are to regulate cell cycle, initiate apoptosis and repair DNA [1, 2]. Active p53 also plays a pivotal role in maintaining genomic integrity of cells and preventing tumor development. In normal cells, the level of p53 is tightly regulated by the oncoprotein MDM2 via a key negative feed back loop [3, 4]. Indeed, the loss of p53 wild-type activity in cancer cells is due to two common mechanisms: one is point mutations in P53 genes, another is functional inhibition by negative regulator MDM2 [5]. Recent studies suggested that the restoration of endogenous p53 activity can efficiently inhibit the growth of cancer cells [6]. Thus, chemical compounds capable of activating p53 signal pathway are considered to be a new class of promising anticancer drugs.

The structural basis of the p53–MDM2 interaction has been well studied [7]. X-ray structures show that p53 peptides prefer a helical structure in the p53–MDM2 complexes [7–9]. P53 interacts with MDM2 by inserting its hydrophobic face (Phe19, Trp23, and Leu26) into a deep hydrophobic groove of MDM2 [10, 11], thus direct disruption on the binding of p53 to MDM2 may be an attractive pathway for anticancer therapy [12, 13]. According to the X-ray structure, the inhibitors were designed by mimicking the interaction of the three residues in p53 with MDM2 for the high binding affinities. For example, peptide inhibitors designed by several groups display high binding affinities for MDM2 [14–19], and several classes of non-peptide small molecule compounds

J. Chen (✉)
School of Science, Shandong Jiaotong University, Jinan 250014,
China
e-mail: chenjianzhong1970@163.com; jzchen1970@gmail.com

J. Wang · W. Zhu
Shanghai Institute of Materia Medica, Drug Discovery and
Design Center, Chinese Academy of Sciences, 555 Zuchongzhi
Road, Shanghai 201203, China

G. Li (✉)
Laboratory of Molecular Modeling and Design, State Key
Laboratory of Molecular Reaction Dynamics, Dalian Institute of
Chemical Physics, Chinese Academy of Science, Dalian, China
e-mail: ghli@dicp.ac.cn

reported to date, such as the cis-imidazolines (nutlins) [20], isoindolinone [21], spiro-oxindoles (MI-63) [22–24], and benzodiazepinedions derivatives [25], also strongly compete with p53 for binding to MDM2.

Crystal structures of protein complexes provide an important starting point for quantitative understanding of the binding mechanism. Many computational studies have been performed on the p53–MDM2 interaction. Ding et al. [26] carried out quantum mechanics calculations on the p53–MDM2 complex to study residue-specific interactions, and their results suggested that van der Waals interactions control the p53–MDM2 binding. The studies of binding free energy calculations from other groups based on MD simulations also yielded similar conclusions to Ding et al. [27–29]. Computational alanine-scanning mutagenesis used by several groups showed that four key position mutations (Phe19, Leu22, Trp23 and Leu26) of p53 resulted in a significant decrease in binding free energies [30–32]. Besides the binding free energy, the protein conformational change induced by ligand binding is also very important to guide rational drug design. Espinoza-Fonseca et al. [33] applied MD simulation to probe the conformation changes of MDM2, and their results revealed that the most flexible region of MDM2 is the p53-binding cleft. Although these computational studies and crystal structures have improved the understanding of the molecular basis for the inhibition of the p53–MDM2 interaction, dynamic information on the conformation changes of MDM2 induced by p53 and inhibitor bindings are still essential for characterizing functionally significant motions in MDM2.

Recent studies have shown that biologically important concerted motions can be extracted from MD simulation trajectory by using cross-correlation analysis [34] and principal component analysis (PCA) [35–37]. In fact, it is increasingly becoming clear that the underlying dynamics of conformation changes of proteins are critical [38]. Towards this goal, MD simulations were extensively applied to investigate the biochemical phenomena [39–43]. In this work, p53 and two inhibitors P4 and MI63-analog (MI63a) were chosen to explore the conformation changes of MDM2 induced by their bindings using PCA and binding free energy calculations based on MD simulations. P4 is a peptide inhibitor (LTFEHYWAQLTS) designed by Czarna et al. [44], and structurally shares three key residues (Phe19, Trp23 and Leu26) with p53 (Fig. 1a, b). This inhibitor shows strong inhibition potency (K_i value of 4 nM) on the p53–MDM2 interaction [44]. MI-63 and MI-219 are the best optimized derivatives of the spiro-oxindole group (K_i values of 5–6 nM) [22], while MI63a is an analog of non-peptide inhibitor (MI-63), and shares structures from the common spiro-oxindole group with MI-63 (Fig. 1c). MI63a can also produce potent inhibiting effects (K_i value of 36 nM) on the p53–MDM2 interaction [45].

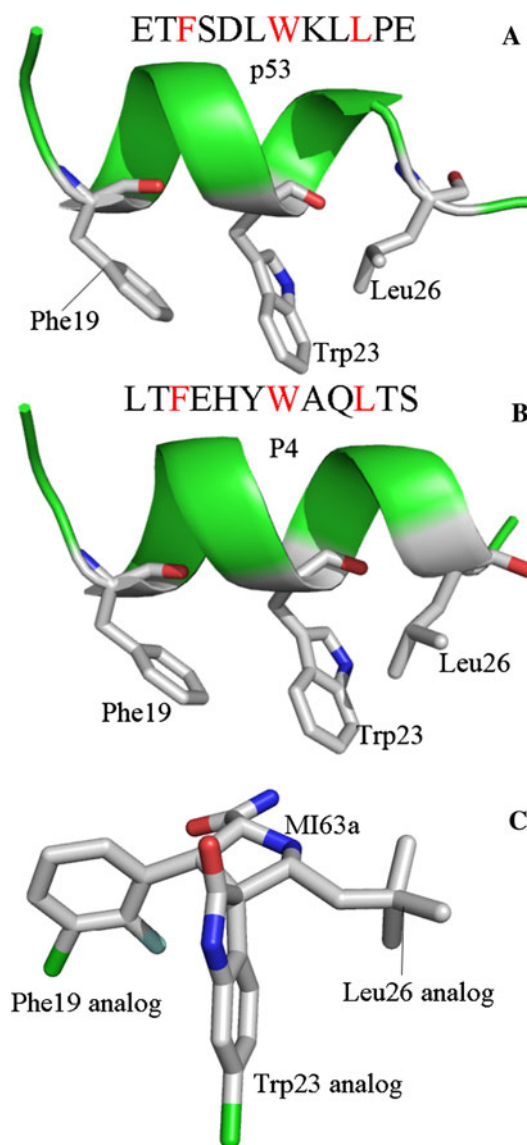


Fig. 1 Molecular structures of three binding partners: **a** p53, **b** peptide inhibitor P4, **c** non-peptide inhibitor MI63a. The residue Phe19, Trp23, Leu26 and MI63a are shown in sticks

This study helps to clarify the molecular basis of the inhibition of the p53–MDM2 interaction. We also expect that the results of this study will provide significant contributions to anticancer drug designs targeting the p53–MDM2 interaction.

Theory and method

System preparation

The crystal structures of MDM2 complexed with p53, MI63a and P4 were obtained from the Protein Data Bank

(PDB entry: 1YCR for p53–MDM2 [7], 3G03 for P4–MDM2 [44] and 3LBL for MI63a–MDM2 complexes [45]). The structure of unbound MDM2 was obtained by removing p53 from 1YCR. Due to difference in the lengths of protein and peptide structures, the residues 25–109 of MDM2 and the first 11 residues in p53 and P4 were used for our simulations. The amino terminus and carbonyl terminus MDM2 and peptides were capped by an acetyl (ACE) and an N-methyl group (NME), respectively. All crystal water molecules were kept in the starting model. All of the missing hydrogen atoms were added with the leap module in the Amber 12 software package [46]. The ff03 force field was applied to obtain the force field parameters for three proteins and water molecules [47]. The structure of MI63a was minimized at the semiempirical AM1 level, and the AM1-BCC charges were assigned to MI63a by the AM1-BCC program [48, 49]. The force field parameters of MI63a were generated by the general Amber force field (GAFF) [50]. The complex was solvated in an octahedron-link TIP3P water box, and the system was neutralized by adding an appropriate number of counterions.

MD simulations

To remove any steric clashes, the initial structure was relaxed in 5,000 steps with constraint on the complex, followed by full minimization of another 5,000 steps without any constraints. Then, the system was heated from 0 to 300 K in 300 ps, and equilibrated at 300 K for another 300 ps. After minimization and heating, a 30-ns production MD simulation without restriction was performed on the system at a constant temperature of 300 K and a constant pressure of 1 atm. During MD simulation, the integration time step was set to 2 fs, temperature was regulated using Langevin dynamics with the collision frequency of 2 ps^{-1} . All the covalent bonds involving hydrogen atoms were fixed using SHAKE algorithm [51]. Periodic boundary conditions were used to avoid edge effects, and particle mesh Ewald method was applied to treat the long-range electrostatic interaction [52, 53]. The cutoff distance for the long-range electrostatic and van der Waals energy terms was set to 10.0 Å.

PCA analysis

PCA is an important tool for insights into conformation change of proteins. In this paper, the Ptraj module [54] of the Amber software tool was used for PCA analysis. Correlated motions were probed by performing cross-correlation analysis on dynamics trajectory, and the cross-correlation coefficient c_{ij} for each pair of C_α atoms i and j were obtained by the following equation.

$$c_{ij} = \frac{\langle \Delta r_i \Delta r_j \rangle}{(\langle \Delta r_i^2 \rangle \langle \Delta r_j^2 \rangle)^{1/2}} \quad (1)$$

Where Δr_i is the displacement from the mean position of the i th atom, and the angle bracket represents the time average over the equilibrated trajectory. Furthermore, the collective motions of MDM2 were also addressed by using the positional covariance matrix C of atomic coordinates and its eigenvectors [35]. The elements of the positional covariance matrix C were determined by Eq. 2.

$$C_i = \langle (q_i - \langle q_i \rangle)(q_j - \langle q_j \rangle) \rangle \quad (i, j = 1, 2, \dots, 3N) \quad (2)$$

in which q_i is the Cartesian coordinate of the i th C_α atom, and N is the number of C_α atom considered. The average is calculated over the equilibrated trajectory after superimposition on a reference structure to remove overall translations and rotations by using a least-square fit procedure [36]. The matrix C is symmetric and can be diagonalized by an orthogonal coordinate transformation matrix T , which transforms it into a diagonal matrix Λ of eigenvalues λ_i :

$$\Lambda = T^T C T \quad (3)$$

where the columns are the eigenvectors corresponding to the direction of motion relative to $\langle q_i \rangle$, and each eigenvector associated with an eigenvalue that represents the total mean-square fluctuation of the system along the corresponding eigenvector.

Calculation of binding free energy

Binding free energies of p53 and two inhibitors to MDM2 were calculated using the parallelized python script *MMPBSA.py.MPI* in Amber 12 [55]. For each complex, a total number of 200 snapshots for this calculation were taken from the last 10 ns of MD trajectory with an interval of 50 ps. In this method, the binding free energy (ΔG) can be represented as:

$$\Delta G = \Delta E_{MM} + \Delta G_{sol} - T\Delta S \quad (4)$$

where ΔE_{MM} and $T\Delta S$ are the molecular mechanics free energy and the conformational entropy effect in the gas phase, respectively, and ΔG_{sol} is the solvation free energy. ΔE_{MM} can be further divided into two parts:

$$\Delta E_{MM} = \Delta E_{ele} + \Delta E_{vdw} \quad (5)$$

in which ΔE_{ele} and ΔE_{vdw} represent the contributions from the electrostatic and van der Waals interactions, respectively. The solvation free energy (ΔG_{sol}) can be expressed as:

$$\Delta G_{sol} = \Delta G_{pol} + \Delta G_{nonpol} \quad (6)$$

where ΔG_{pol} and ΔG_{nonpol} are the polar and non-polar contributions to the solvation free energy, respectively. ΔG_{pol} is calculated using the modified GB model developed by Onufriev et al. [56]. To this aim, the dielectric constants in the protein and solvent were set to 1.0 and 80.0, respectively [57]. The ionic strength was set to 0.15 M, and the other parameters were set to default values [42]. ΔG_{nonpol} was estimated by

$$\Delta G_{nonpol} = \gamma SASA + \beta \quad (7)$$

where the symbol *SASA* denotes the solvent accessible surface area which was computed using a probe radius of 1.4 Å with a fast linear combination of pairwise overlap (LCPO) algorithm [58]. In this work, the values for γ and β were set to 0.0072 kcal mol⁻¹ Å⁻² and 0.0 kcal mol⁻¹, respectively [57].

The contributions of entropy ($T\Delta S$) to the binding free energy arises from changes in the translational, rotational and vibrational degrees of freedom, as follows

$$\Delta S = \Delta S_{translational} + \Delta S_{rotational} + \Delta S_{vibrational} \quad (8)$$

in which the first two terms can be calculated using classical statistical thermodynamics, and the contribution from the vibrational degrees of freedom calculated by normal-mode analysis using the program *mmpbsa_py_nabnmode* in Amber 12. 200 snapshots were selected from the last 10 ns of the MD trajectory with an interval of 50 ps, each snapshot was minimized using a maximum of 50,000 steps and a root-mean-square (rms) gradient of 10⁻⁴ kcal mol⁻¹ Å⁻¹.

Results and discussions

Stability of MD simulation

To evaluate the reliability of MD simulation equilibrium, the root mean square deviation (RMSD) of the backbone atoms relative to the corresponding crystal structure during simulations were calculated and depicted in Fig. 2. According to Fig. 2, all systems have reached equilibrium after 15 ns of MD simulations. The average RMSD of the backbone atoms after the equilibration are 1.30, 1.25 and 1.22 Å for MDM2 complexed with p53, P4 and MI63a, respectively, and 1.42 Å for the unbounded MDM2. All RMSD deviations from the mean are lower than 0.59 Å. This result shows that the equilibrium of MD simulation is reliable, and also basically agrees with the fact that the unbound form of MDM2 is more dynamics and less stable compared to the bounded form of MDM2 [31, 33].

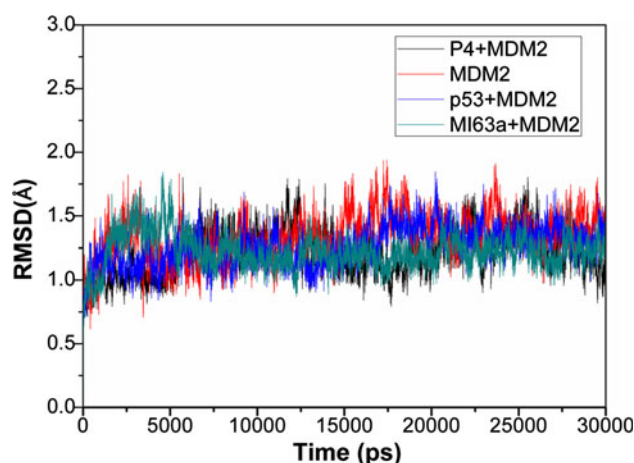


Fig. 2 The root-mean-square deviations (RMSD) of the backbone atoms relative to the corresponding crystal structures as function of time

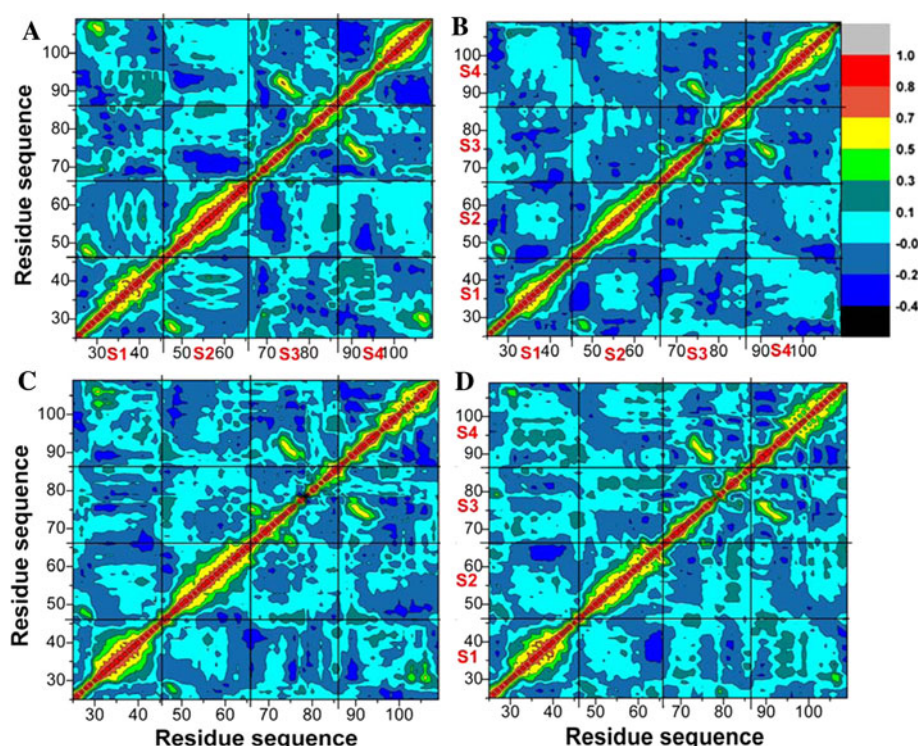
Cross-correlation analysis

To obtain insight into the effect of p53 and two inhibitor bindings on the dynamics of MDM2, the cross-correlation matrices of the fluctuations were calculated and plotted in Fig. 3. Highly positive regions (red and yellow) are associated with strong correlated motions of specific residues, whereas negative regions (dark blue) are indicative of strong anti-correlation in the specific residue movements. The results show that there are very few highly correlated motions except for the diagonal square, which reflects the correlation of a residue with itself. However, the anti-correlated motions (blue and dark blue) were obviously decreased in the presence of p53 and two inhibitors (shown in Fig. 3a–d).

In the case of the unbounded MDM2, the obvious anticorrelated motions are observed in the subunit S4, and the strong anticorrelated motions of intersubunits (off-diagonal square) are noted between the subunits S2 and S3. The subunits S3 and S4 also produce weak anti-correlated motion relative to the subunit S1. Additionally, an obvious correlated motion also occurs between the subunits S3 and S4 (red and yellow).

As seen from Fig. 3, the binding of p53 and two inhibitors induces similar correlation motions in specific residues of MDM2. In comparison with unbound MDM2, the presence of p53 and two inhibitors results in an obvious decrease of anticorrelated motions in the subunit S4. In addition, intersubunit anticorrelated motions were almost disappeared between the subunits S2 and S3, and the intersubunit correlated motions between subunits S3 and S4 were decreased by the binding of three partners. However there are also some differences in the motions induced by the presence of different partners. For example, the anti-correlated motions of the subunit S2 relative to S1 were

Fig. 3 Cross-correlation matrices of the fluctuations of the coordinates for C_α atoms around their mean positions after the equilibrium of MD simulation. The extent of correlated motions and anticorrelated motions are color-coded for unbound MDM2 (a), the p53–MDM2 complex (b), the P4–MDM2 complex (c) and the MI63a–MDM2 complex (d)



strengthened in the presence of p53 and MI63a, while the anticorrelated motions of the subunits S3 and S4 relative to S1 were disappeared due to the binding of MI63a.

The above cross-correlation analysis showed that the correlated and anticorrelated motions of MDM2 are significantly affected by the presence of binding partners. The differences in the motions reflect the rearrangement of the residues due to the presence of the different structural binding partner. As seen from the Fig. 3, the changes in the correlated motion nearby Gln72, Asp80, Val93 and Tyr100 are very obvious. This result implies that the conformations nearby these residues are highly changed.

Principal component analysis

In order to understand the changes of motions in more details, PCA based on the trajectory of MD simulation were performed. Figure 4 shows a plot of the eigenvalues obtained from the diagonalization of the covariance matrix of the atomic fluctuations, depicted in decreasing order versus the corresponding eigenvector indices for the three complexes. As seen from Fig. 4, the first few eigenvalues are relative to concerted motions, and quickly decreased in amplitude to reach a number of constrained, more localized fluctuations. The first five principal components (PC) account for 62, 55, 63 and 58 % of the motion observed in the last 15 ns of the trajectory for the unbounded MDM2 and the complexes with p53, P4 and MI63a, respectively.

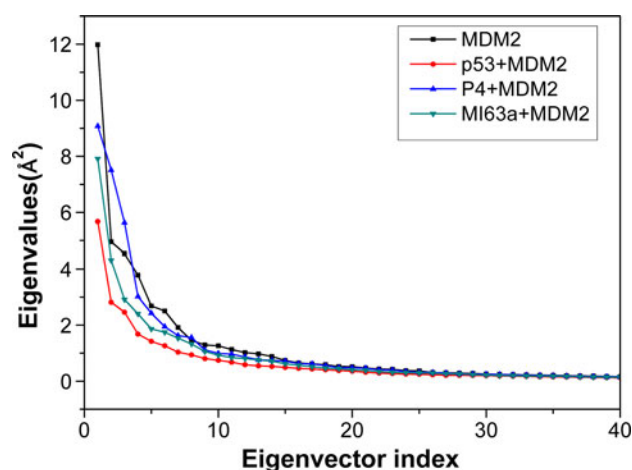
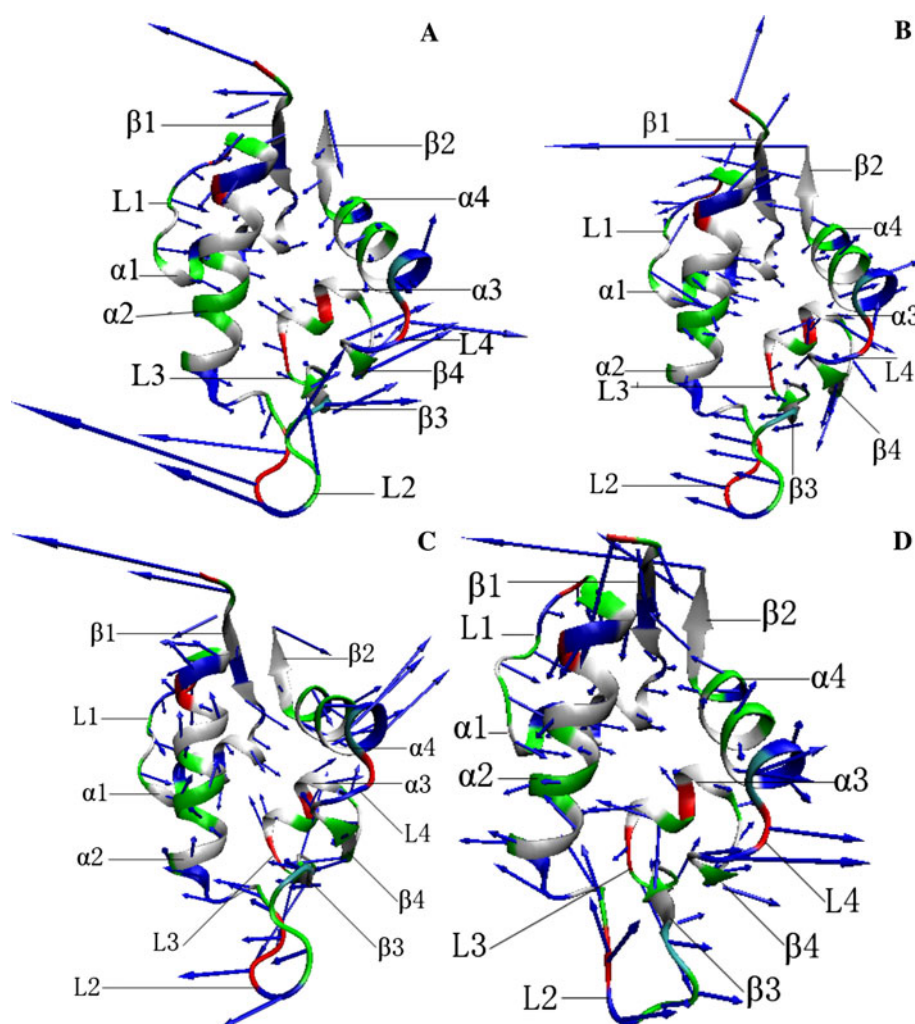


Fig. 4 Comparison of the eigenvalues plotted against the corresponding eigenvector indices obtained from the C_α covariance matrix constructed from the equilibrium phase of MD simulations

According to Fig. 4, the properties of the motions described by the first few PCs are different for the four systems. The magnitudes of the eigenvalues of MDM2 with the three binding partners are lower than that of the unbounded MDM2. The effect of three partner bindings on the motion is also not the same. The magnitude of PC1 was drastically decreased in the presence of p53 and MI63a, while the magnitude of PC2 and PC3 is greatly decreased by the P4 binding.

To qualitatively understand the movement direction of each part of MDM2, the first eigenvectors describing

Fig. 5 Collective motions corresponding to PC1 obtained by performing principal component analysis (PCA) on MD simulation trajectory after the equilibrium. **a** Unbound MDM2, **b** the p53–MDM2 complex, **c** the P4–MDM2 complex, **d** the MI63a–MDM2 complex



correlated motion of residues were obtained by performing the PCA on the MD trajectory and plotted in Fig. 5 with the structure of MDM2. As shown in Fig. 5, the hydrophobic cleft of MDM2 is composed of the sides (formed by two helices $\alpha 2$ and $\alpha 4$), the bottom (formed by two short helices $\alpha 1$ and $\alpha 3$) and two end caps (formed by the four β sheets). The length of the arrow in each C_{α} atom represents the magnitude of movement, and the direction of the arrow is the direction of movement.

According to Fig. 5, an interesting phenomenon can be noted that the motion of the cleft in unbound MDM2 is significantly different from the motion of MDM2 with the three partners. In details, for the unbound MDM2, the helices $\alpha 2$ and $\alpha 4$ move inward the binding cleft, and the two short helices ($\alpha 1$ and $\alpha 3$) of the cleft bottom move close to each other. It is also observed that β sheets ($\beta 3$ and $\beta 4$) run toward the helix $\alpha 4$. All the above modes of motion tend to make the binding cleft narrower. These results basically agree with the NMR study reported by Uhrinova et al. [59] and the conformation analysis performed by Paul Barrett et al. [60] using dynamite software.

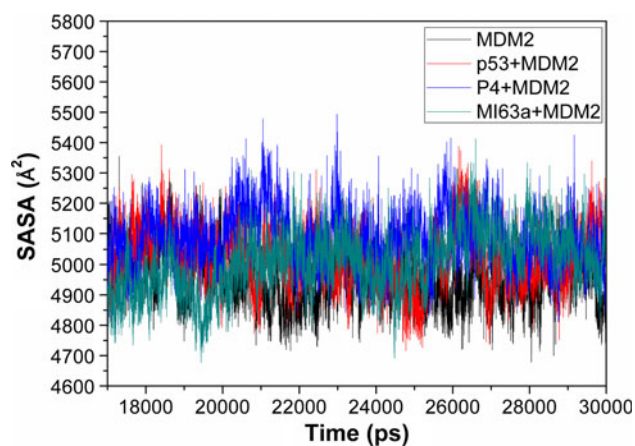


Fig. 6 Plot of the average surface area of MDM2 computed through the equilibrium phase of MD simulation

As seen from Fig. 5, the presence of the three binding partners induces an outer movement of two helices $\alpha 2$ and $\alpha 4$ away from the cleft. In the case of P4 and p53 bindings, the $\beta 3$ and $\beta 4$ have a tendency to move away from the

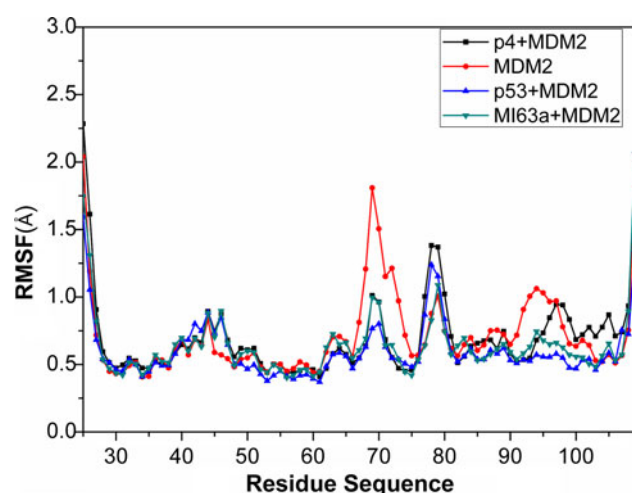


Fig. 7 Plot of the RMSF of C α atoms in MDM2 through the equilibrium phase of MD simulation

helix $\alpha 4$, while in the case of the MI63a binding, the $\beta 3$ and $\beta 4$ move outwards. The above analysis suggests that the presence of the three binding partners tends to make the binding cleft of MDM2 wider and bigger so as to accommodate these partners. To confirm this result, the surface area of MDM2 was calculated by using the LCPO algorithm of Weiser et al. [58], and plotted in Fig. 6. The results showed that the average surface area of unbounded MDM2 is 4,952 Å², while the ones of MDM2 with p53, P4 and MI63a are 5,017, 5,081 and 5,004 Å², respectively. Indeed the binding of p53, P4 and MI63a leads to an increase in the surface area of MDM2, which suggests that the hydrophobic cleft of MDM2 is adaptive to the different binding partners.

According to Fig. 5, the presence of the three binding partners also produces significant effect on the hinge region (L2) linking $\alpha 2$ and $\beta 3$. The binding of p53 and P4 reduces the magnitudes of the motion in the L2, while the presence of MI63a makes the motion of L2 disordered. Due to the small size of $\beta 3$ (the residues 74–77) and L3 (the residues 79–80), the motion of L2 can greatly affect the motion of $\beta 3$ and L3. In order to confirm this analysis, we calculated the rms fluctuation (RMSF) of C α atoms in MDM2 (shown in Fig. 7). It is observed that the three partner bindings result in an obvious decrease in the RMSF of residues 63–74, and increase the RMSF of residues 77–81 at the same time. The above two analyses are consistent. As seen from Figs. 5 and 7, the motion of the $\beta 4$ and $\alpha 4$ was also changed by the binding of three partners. The RMSF of the residues 91–97 decreases substantially with the binding of the three partners. The binding of P4 increases the RMSF of the residues 100–104. Thus, it is concluded from the above analysis that the binding cleft of MDM2 is very flexible and the binding of three partners favors the

Table 1 Binding free energy and its components for three binding partners complexed with MDM2 in kcal mol^{−1a}

Component	p53	P4	MI63a
ΔE_{ele}	−112.6 (0.3)	−216.5 (0.3)	−9.8 (0.1)
ΔE_{vdw}	−62.5 (0.1)	−64.4 (0.1)	−38.4 (0.1)
ΔG_{nonpol}	−8.7 (0.01)	−8.9 (0.01)	−5.5 (0.01)
ΔG_{pol}	138.9 (0.2)	244.6 (0.3)	20.6 (0.2)
ΔG_{sol}	129.5 (0.1)	235.7 (0.2)	15.2 (0.2)
$\Delta G_{\text{pol+ele}}^a$	25.6 (0.2)	28.2 (0.2)	10.9 (0.1)
$-\Delta S$	37.4 (0.3)	34.2 (0.2)	23.3 (0.2)
ΔG_{bind}	−8.2 (0.1)	−11.0 (0.1)	−9.7 (0.1)
ΔG_{expb}^b	−9.2	−11.5	−10.2

Standard errors of the mean are given in parentheses

^a $\Delta G_{\text{pol+ele}} = \Delta E_{\text{ele}} + \Delta G_{\text{pol}}$

^b Obtained from Refs. [9, 30, 44]

stability of MDM2 conformation. This result is in good agreement with the study of Espinoza-Fonseca et al. [33].

Binding free energy and binding mechanism

To elucidate the effect of the three partner bindings on MDM2 conformation and the binding mechanisms to MDM2 from the viewpoint of energy, the binding free energies were computed by using molecular mechanics generalized Born surface area (MM-GBSA) method. Table 1 shows the binding free energies for the association of p53, P4 and MI63a with MDM2. The corresponding binding free energies are −8.2, −11.0 and −9.7 kcal mol^{−1}, respectively. It is observed that the rank of our predicted binding free energies is in agreement with the experimentally determined rank, and the three predicted binding free energies are even quantitatively close to the experimental values. Thus, this result suggests that the current analysis by MM-GBSA is reliable.

The individual components contributing to the binding free energy are provided in Table 1. The components favoring binding are those from the van der Waals interactions ΔE_{vdw} of three binding partners (−38.4 to −64.4 kcal mol^{−1}) with MDM2, the non-polar solvation energy ΔG_{nonpol} involving the hydrophobic effect (−5.5 to −8.9 kcal mol^{−1}), and the intermolecular electrostatic interactions ΔE_{ele} (−9.8 to −216.5 kcal mol^{−1}) between the partners and MDM2. The most negative value for ΔE_{ele} is the P4–MDM2 complex (−216.5 kcal mol^{−1}), followed by the p53–MDM2 (−112.6 kcal mol^{−1}) and the MI63a–MDM2 complex (−9.8 kcal mol^{−1}).

Intermolecular electrostatic interactions involve contributions from hydrogen bonds and others polar contacts between the binding partners and MDM2. Thus, the strength of electrostatic interactions might be related to the

Table 2 The hydrogen bonds of the key residues

Complex	Donor	Acceptor	Distance ^a / Å	Angle ^a / (°)	Freq. ^b / %
p53–MDM2	Phe19-N-H	Gln72-OE1	2.98	148.75	94.20
	Trp23-NE1-HE1	Met54-OE1	2.98	156.06	82.34
P4–MDM2	Phe19-N-H	Gln72-OE1	2.93	149.86	92.82
	Trp23-NE1-HE1	Met54-OE1	2.99	150.62	71.43
MI63a–MDM2	MI63a-N11-H4	Met54-OE1	2.90	158.94	98.81

^a The hydrogen bonds are determined by the acceptor...donor atom distance of <3.5 and acceptor...H-donor angle of >120 Å

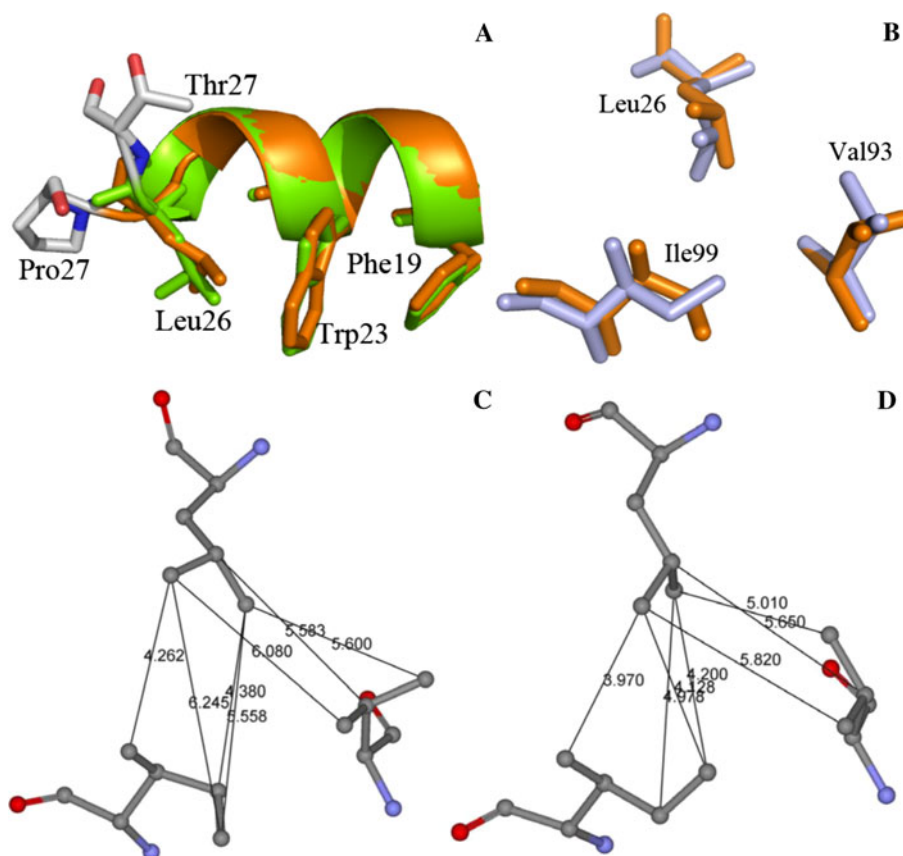
^b Occupancy (%): to evaluate the stability and the strength of the hydrogen bond

corresponding number of hydrogen bonds and polar contacts. The p53–MDM2, P4–MDM2 and MI63a–MDM2 complexes form two, two and one intermolecular hydrogen bonds (Table 2), respectively. According to Table 2, the backbone NH of Phe19 of p53 and P4 provide a hydrogen atom to form a hydrogen bond with the OE1 of Gln72 in MDM2, while this hydrogen bond is lost for MI63a. This result explains the reason behind the binding of P4 and p53

leading to the decrease in the motion magnitude of L2 and the disorder of L2 movement in the MI63A–MDM2 complex (Fig. 5). Structurally, an anti-parallel orientation binding of p53 and P4 to the helix $\alpha 2$ may form a strong dipole–dipole interaction with MDM2 [7], which produce more polar contacts with the binding cleft. The two above interactions clarify the reason why the electrostatic interactions of p53 and P4 with MDM2 are much stronger than MI63a. Although the inhibitor P4 generates stronger electrostatic interactions with MDM2 than p53, this favorable interaction is screened by the more unfavorable desolvation of polar groups.

Intermolecule van der Waals interactions of p53, P4 and MI64a with MDM2 are -62.5 , -64.4 and -38.5 kcal mol^{-1} , which favors in their associations with MDM2. The van der Waals energies ΔE_{vdw} between MDM2 and two binding partners P4 and p53 are increased by 24.0 and 25.9 relative to MI63a, respectively. This is because more van der Waals contacts are formed by the side chains of residues in P4 and p53 with MDM2 compared to MI63a. For the p4–MDM2 complex, the intermolecule van der Waals energy is shifted by -1.9 kcal mol^{-1} relative to the p53–MDM2 complex. To clarify this issue, we performed a superimposition analysis on the conformations of p53 and P4 (Fig. 8). As seen from Fig. 8a, except for the carbonyl terminus, the conformation of P4 agrees well with the one of p53. The difference in the conformations of Pro27 from

Fig. 8 Geometries of key residues: **a** superimposition of p53 and P4 crystal structures, the structures are shown in cartoon, and the p53 and P4 are displayed in green and orange, respectively. Key residues are shown in sticks; **b** key residues shown in sticks, Leu26 belongs to P4 and p53, Val93 and Ile99 are in MDM2, the light blue for P4–MDM2 complex, and the orange for p53–MDM2 complex; **c** distances between key carbon atoms in the p53–MDM2 complex, the residues are shown in ball and sticks; **d** distances between key carbon atoms in the P4–MDM2 complex, the residues are shown in ball and sticks



p53 and Thr27 from P4 might induce the conformation shift of Leu26 (p53 and P4), which in turn changes the orientations and positions of key residues in MDM2 relative to p53 and P4. Figure 8b shows that the conformation orientation of the residues Val93 and Ile99 tends to decrease the number of van der Waals contacts with Leu26 for the p53–MDM2 complex. To support this issue, the distances between key carbon atoms are depicted in the lowest energy structure from the MD trajectory (Fig. 8c, d). For the P4–MDM2 complex, the distances between the key carbon atoms in Leu26 and the residues Val93 and Ile99 are shortened relative to the p53–MDM2 complex, which shows that Leu26 of P4 can produce stronger van der Waals interactions with MDM2 than p53. This analysis accounts for the binding of P4 producing more obvious effect on the motions of helix $\alpha 4$ than the other two binding partners (Figs. 5c, 7).

Formation of a protein complex is in general opposed by a loss in conformation entropy of the binding partners [61]. The entropy contributions induced by p53, P4 and MI63a bindings are in the range of 23.3–37.4 kcal mol⁻¹. For the p53–MDM2 complex, the current predicted entropic contribution is in agreement with the studies from Joseph et al. [62]. Interestingly, the entropic effects of p53 and P4 bindings are highly large compared to MI63a. The large entropic effects mainly arise from the changes in the conformational freedom of the binding partners. The inhibitor MI63a exhibits 10 rotatable bonds, but the side chains of key residues in p53 and P4 have rotatable bonds much more than 10. The rotation around these bonds will be more restricted in the presence of than the absence of MDM2, resulting in a decrease in the entropy upon binding.

We concluded from the above analysis that the unfavorable desolvation of polar groups weakens the binding of the three partners. As seen from Table 1, this unfavorable force is partially compensated by favorable electrostatic interactions, which has been observed by studies of other systems [42, 63–65]. The electrostatic interaction and van der Waals interactions of MDM2 with p53 and P4 are much stronger than MI63a. This implies that there may be additional interactions between MDM2 and those two peptides. Analysis of the X-ray structure of the p53–MDM2 complex testifies that in addition to Phe19, Trp23, and Leu26 in p53, a fourth residue Leu22 also provides a significant contributions to the overall interaction between MDM2 and p53 [7]. A quantum mechanical calculation on the p53–MDM2 interaction from Ding et al. [26] also supports this hypothesis. X-ray crystallography of the P4–MDM2 complex reveals that the residue Tyr22 in P4 also plays a similar role to Leu22 in p53 [44]. The information obtained in this part is expected to be helpful to the rational

design of non-peptide small molecules inhibiting the p53–MDM2 interactions.

Conclusion

Four 30-ns MD simulations have been performed on unbound MDM2 and MDM2 with binding partners (p53, P4 and MI63a) to probe the effect of their bindings on the conformational change of MDM2. This study reveals that the bind cleft in MDM2 is highly flexible, and the size and shape of this cleft changes with the presence of different structural binding partners. The cross-correlation analysis also suggests that the presence of three binding partners can produce significant effect on the correlated and anti-correlated motion of MDM2. Binding free energies were calculated to provide further information on the binding modes of the three partners to MDM2. The understanding of the dynamics involved the p53-binding cleft is of high significance not only in insight into the biological relevance of MDM2, but also in the rational design of anti-cancer drugs.

Acknowledgments This work is supported by the National Natural Science Foundation of China (11104164, 11274206 and 31200545), Dr. Start-up Foundation of Shandong Jiaotong University and Natural Science Foundation of Shandong Jiaotong University.

References

- Harris SL, Levine AJ (2005) *Oncogene* 24(17):2899
- Fridman JS, Lowe SW (2003) *Oncogene* 22(56):9030
- Stott FJ, Bates S, James MC, McConnell BB, Starborg M, Brookes S, Palmero I, Ryan K, Hara E, Vousden KH (1998) *EMBO J* 17(17):5001
- Unger T, Juven-Gershon T, Moallem E, Berger M, Sionov RV, Lozano G, Oren M, Haupt Y (1999) *EMBO J* 18(7):1805
- Nikolova PV, Wong KB, DeDecker B, Henckel J, Fersht AR (2000) *EMBO J* 19(3):370
- Vousden KH, Lane DP (2007) *Nat Rev Mol Cell Biol* 8(4):275
- Kussie PH, Gorina S, Marechal V, Elenbaas B, Moreau J, Levine AJ, Pavletich NP (1996) *Science* 274(5289):948
- Chen HF, Luo R (2007) *J Am Chem Soc* 129(10):2930
- Popowicz GM, Czarna A, Rothweiler U, Schwagierczak A, Krajewski M, Weber L, Holak TA (2007) *Cell Cycle* 6(19):2386
- Moll UM, Petrenko O (2003) *Mol Cancer Res* 1(14):1001
- Chi SW, Lee SH, Kim DH, Ahn MJ, Kim JS, Woo JY, Torizawa T, Kainosho M, Han KH (2005) *J Biol Chem* 280(46):38795
- Chène P (2003) *Nat Rev Cancer* 3(2):102
- Klein C, Vassilev L (2004) *Br J Cancer* 91(8):1415
- Grönroos E, Terentiev AA, Punga T, Ericsson J (2004) *Proc Natl Acad Sci USA* 101(33):12165
- Kritzer JA, Lear JD, Hodsdon ME, Schepartz A (2004) *J Am Chem Soc* 126(31):9468
- Lee JH, Zhang Q, Jo S, Chai SC, Oh M, Im W, Lu H, Lim HS (2011) *J Am Chem Soc* 133:676
- Phan J, Li Z, Kasprzak A, Li B, Sefti S, Guida W, Schönbrunn E, Chen J (2010) *J Biol Chem* 285(3):2174

18. Liu M, Li C, Pazgier M, Mao Y, Lv Y, Gu B, Wei G, Yuan W, Zhan C (2010) *Proc Natl Acad Sci USA* 107(32):14321
19. Pazgier M, Liu M, Zou G, Yuan W, Li C, Li J, Monbo J, Zella D, Tarasov SG (2009) *Proc Natl Acad Sci USA* 106(12):4665
20. Vassilev LT, Vu BT, Graves B, Carvajal D, Podlaski F, Filipovic Z, Kong N, Kammlott U, Lukacs C, Klein C (2004) *Science* 303(5659):844
21. Hardcastle IR, Ahmed SU, Atkins H, Farnie G, Golding BT, Griffin RJ, Guyenne S, Hutton C, Källblad P, Kemp SJ (2006) *J Med Chem* 49(21):6209
22. Ding K, Lu Y, Nikolovska-Coleska Z, Wang G, Qiu S, Shangary S, Gao W, Qin D, Stuckey J, Krajewski K (2006) *J Med Chem* 49(12):3432
23. Shangary S, Wang S (2009) *Annu Rev Pharmacol Toxicol* 49:223
24. Shangary S, Qin D, McEachern D, Liu M, Miller RS, Qiu S, Nikolovska-Coleska Z, Ding K, Wang G, Chen J (2008) *Proc Natl Acad Sci USA* 105(10):3933
25. Grasberger BL, Lu T, Schubert C, Parks DJ, Carver TE, Koblish HK, Cummings MD, LaFrance LV, Milkiewicz KL, Calvo RR (2005) *J Med Chem* 48(4):909
26. Ding Y, Mei Y, Zhang JZH (2008) *J Phys Chem B* 112(36):11396
27. Hu G, Wang D, Liu X, Zhang Q (2010) *J Comput Aid Mol Des* 24(8):687
28. Lu SY, Jiang YJ, Zou JW, Wu TX (2011) *J Mol Graph Model* 30:167
29. Chen J, Wang J, Xu B, Zhu W, Li G (2011) *J Mol Graph Model* 30:46
30. Massova I, Kollman PA (1999) *J Am Chem Soc* 121(36):8133
31. Zhong H, Carlson HA (2005) *Proteins* 58(1):222
32. Chen J, Zhang D, Zhang Y, Li G (2012) *Int J Mol Sci* 13(2):2176
33. Espinoza-Fonseca L, Trujillo-Ferrara JG (2006) *Biopolymers* 83(4):365
34. Ichiye T, Karplus M (2004) *Proteins* 11(3):205
35. Levy R, Srinivasan A, Olson W, McCammon J (2004) *Biopolymers* 23(6):1099
36. Laberge M, Yonetani T (2008) *Biophys J* 94(7):2737
37. Amadei A, Linssen A, Berendsen HJC (2004) *Proteins* 17(4):412
38. Boehr DD, Nussinov R, Wright PE (2009) *Nat Chem Biol* 5(11):789
39. Wang J, Yang H, Zuo Z, Yan X, Wang Y, Luo X, Jiang H, Chen K, Zhu W (2010) *J Phys Chem B* 114(46):15172
40. Wu EL, Han KL, Zhang JZH (2008) *Chem A Eur J* 14(28):8704
41. Chen J, Zhang S, Liu X, Zhang Q (2010) *J Mol Model* 16(3):459
42. Kar P, Knecht V (2012) *J Phys Chem B* 116(8):2605
43. Meher BR, Wang Y (2012) *J Phys Chem B* 116(6):1884
44. Czarna A, Popowicz GM, Pecak A, Wolf S, Dubin G, Holak TA (2009) *Cell Cycle* 8(8):1176
45. Popowicz GM, Czarna A, Wolf S (2010) *Cell Cycle* 9(6):1104
46. Case DA, Darden TA, Cheatham III TE, Simmerling CL, Wang J, Duke RE, Luo R, Walker RC, Zhang W, Merz KM, Roberts S, Hayik S, Roitberg A, Seabra G, Swails J, Götz AW, Kolossváry I, Wong KF, Paesani F, Vanicek J, Wolf RM, Liu J, Wu X, Brozell SR, Steinbrecher T, Gohlke H, Cai Q, Ye X, Wang J, Hsieh M-J, Cui G, Roe DR, Mathews DH, Seetin MG, Salomon-Ferrer R, Sagui C, Babin V, Luchko T, Gusarov S, Kovalenko A, Kollman PA (2012) *AMBER 12*, University of California, San Francisco
47. Duan Y, Wu C, Chowdhury S, Lee MC, Xiong G, Zhang W, Yang R, Cieplak P, Luo R, Lee T (2003) *J Comput Chem* 24(16):1999
48. Jakalian A, Jack DB, Bayly CI (2002) *J Comput Chem* 23(16):1623
49. Jakalian A, Bush BL, Jack DB, Bayly CI (2000) *J Comput Chem* 21(2):132
50. Wang J, Wolf RM, Caldwell JW, Kollman PA, Case DA (2004) *J Comput Chem* 25(9):1157
51. Coleman TG, Mesick HC, Darby RL (1977) *Ann Biomed Eng* 5(4):322
52. Darden T, York D, Pedersen L (1993) *J Chem Phys* 98:10089
53. Essmann U, Perera L, Berkowitz ML, Darden T, Lee H, Pedersen LG (1995) *J Chem Phys* 103(19):8577
54. Case DA, Cheatham TE, Darden T, Gohlke H, Luo R, Merz KM, Onufriev A, Simmerling C, Wang B, Woods RJ (2005) *J Comput Chem* 26(16):1668
55. Miller BR III, McGee TD, Swails JM, Homeyer N, Gohlke H, Roitberg AE (2012) *J Chem Theory Comput* 8(9):3314
56. Onufriev A, Bashford D, Case DA (2004) *Proteins* 55(2):383
57. Gohlke H, Kiel C, Case DA (2003) *J Mol Biol* 330(4):891
58. Weiser J, Shenkin PS, Still WC (1999) *J Comput Chem* 20(2):217
59. Uhrinova S, Uhrin D, Powers H, Watt K, Zheleva D, Fischer P, McInnes C, Barlow PN (2005) *J Mol Biol* 350(3):587
60. Barrett CP, Hall BA, Noble MEM (2004) *Acta Cryst* 60(12):2280
61. Campos SR, Machuqueiro M, Baptista AM (2010) *J Phys Chem B* 114(39):12692
62. Joseph TL, Madhumalar A, Brown CJ, Lane DP, Verma C (2010) *Cell Cycle* 9(6):1167
63. Chen J, Yang M, Hu G, Shi S, Yi C, Zhang Q (2009) *J Mol Model* 15(10):1245
64. Chong LT, Duan Y, Wang L, Massova I, Kollman PA (1999) *Proc Natl Acad Sci USA* 96(25):14330
65. Xu Y, Wang R (2006) *Proteins* 64(4):1058